

# Using Molecular Modeling Methods to Predict the Aluminum Distribution in the Chabazite Zeolite with the Presence of Organic Structure Directing Agents.

Xiaoyu Wang, Yujia Wang, Edward Maginn, and William Schneider\*

*Department of Chemical and Biomolecular Engineering, University of Notre Dame, Notre Dame, IN 46556 USA*

E-mail: wschneider@nd.edu

## Abstract

The catalytic properties of zeolites, which are primarily determined by the framework topology and active centers (e.g.  $\text{Ti}^{4+}$ ,  $\text{Sn}^{4+}$  or  $\text{Al}^{3+}$ ), remain challenging to be controlled in zeolite synthesis. Here, we combined first-principal and classical molecular simulations to investigate how Al siting, and OSDA orientation impacts the energy of a zeolite supercell. 36 T-site CHA zeolite with  $\text{TMAda}^+$  (OSDA) was chosen as the model system. By applying a Boltzmann factor to each Al configuration and as a function of  $\text{TMAda}^+$  orientation, we came to the conclusion Al pairs prefer to locate in 8-MRs compared to 6-MR, 4-MR and D6R, which is consistent with our previous experimental finding. We also found that the potential energy was governed by the distance between the anionic  $\text{AlO}_4^-$  tetrahedra and the cationic quaternary ammonium groups (the Al-N distance), which is the key factor in determining the Al distribution. These results highlight opportunities of using classical molecular simulation combined

with partial charges to represent electrostatic interactions, which enables a promising methodology to exploit the Al distribution and the OSDA orientation in larger supercell systems.

# 1 Introduction

Zeolites are porous crystalline aluminosilicates with different three-dimensional architectures formed by the linking of oxygen atoms of  $\text{AlO}_4^-$  and  $\text{SiO}_4$  tetrahedra to form a covalent network structure.<sup>1</sup> Due to the fact that their pores are of molecular dimensions, zeolites can act as molecular sieves, which enables their application in separation processes.<sup>2-5</sup> The aluminum atoms serve as Brønsted acid sites, which lends zeolites catalytic activity for hydrocarbon cracking, alkylation, and isomerization.<sup>6</sup> Haag et al. reported high turnover rates of several hydrocarbon reactions with increasing concentration of aluminum sites.<sup>7</sup> Even in the low Al-concentration of Si-rich zeolites,  $\text{AlO}_4^-$  provides shape-selective effects in catalysis reactions when sitting at certain positions inside cavities.<sup>8</sup>

It has been estimated that the introduction of zeolites to refining operations has resulted in a  $\sim 30\%$  increase in gasoline yield, making zeolites one of the most important materials in petrochemical processing.<sup>9</sup> Compared with natural zeolites, synthetic zeolites comprise over 70% of the global market, which was valued at 29.08 billion USD in 2016.<sup>10</sup> Synthetic zeolites are typically made under hydrothermal conditions using special organic structure directing agents (OSDAs) that help steer the self-assembly process toward a particular pore shape and Al distribution.<sup>11</sup> It has been estimated that there are millions of potential zeolite frameworks,<sup>12</sup> but only a fraction of these have been actually synthesized. For this reason, a great deal of experimental and theoretical work has been done to better understand the complex process in which different synthesis conditions and OSDAs lead to different zeolite structures.<sup>13-20</sup>

The  $\text{AlO}_4^-$  tetrahedra groups in zeolites are proton active sites, which enables them to be distinguished from other tetrahedra-sites (T-sites) in their surrounding chemical environ-

ment.  $^{27}\text{Al}$  magic angle spinning nuclear magnetic resonance (MAS NMR) can be used to characterize and distinguish tetrahedrally and octahedrally coordinated Al locations. Sklenak et al. used quantum mechanics/molecular mechanics (QM/MM) calculations along with  $^{27}\text{Al}$  multiple quantum MAS NMR to identify chemical shifts of Al sites in MFI-type zeolites.<sup>21–23</sup> Yokoi et al. applied high-resolution  $^{27}\text{Al}$  MAS NMR to distinguish Al sites in different cavities and intersecting channels.<sup>24–26</sup> Al K-edge X-ray adsorption near edge spectroscopy and extended X-ray adsorption fine structure have also been used to differentiate Al-Si and Al-O pairs based on their distances, which provides information on the Al distribution.<sup>27</sup> Rietveld refinement of powder X-ray diffraction is another technique which can locate OSDAs inside zeolite cavities after crystallization.<sup>28–30</sup> Other characterization techniques, including fluorescence spectroscopy,<sup>31</sup> valence-to-core X-ray emission spectroscopy (XES),<sup>32</sup> and atom probe tomography (APT)<sup>33</sup> have been applied to provide information on the relationship between Al siting and the type of OSDA used in synthesis.

Molecular modeling and simulation has also been used to help understand the relationship between OSDA, zeolite structure, and Al siting. Early work focused on using quantum mechanics (QM) and Density Functional Theory (DFT) calculations to explain the acidity of Al sites<sup>34–36</sup> and to develop classical core-shell force fields for modeling the zeolite framework.<sup>37–39</sup> Fletcher et al. used ab initio molecular dynamics (AIMD) to investigate the violation of Löwenstein’s rule with the presence of  $\text{Cu}^+$ .<sup>40</sup> In previous work from our group, AIMD was used to investigate dilute systems consisting of one N,N,N-trimethyl-1-adamantyl ammonium ( $\text{TMAda}^+$ ) OSDA inside chabazite (CHA) frameworks consisting of 36 or 72 tetrahedra sites (T-sites).<sup>41</sup> In a follow-up study, we investigated the influence of alkali cations when co-caging with  $\text{TMAda}^+$ s and compared our theoretical results with existing experiments.<sup>42</sup> The advantage of these type of QM methods is that they obtain the interaction energies between the OSDA and the zeolite framework from first principles. The downside is that the simulations are expensive, such that relatively small systems and short timescales are accessible with current computational resources.

Alternatively, classical simulations with a prescribed force field enable one to simulate relatively large systems and time scales, although the quality of the results depends on the accuracy of the force field used. Lewis et al. developed ZEBEDDE (ZEolites By Evolutionary De nova DEsign), a Monte Carlo code to design suitable OSDAs by docking and growing hydrocarbon chains inside target zeolite frameworks.<sup>43</sup> Burton et al. used molecular modeling to calculate the van der Waals interactions of several quaternary ammonium compounds in zeolite frameworks, including CHA, SSZ-39 (AEI), SSZ-36 (ITE/RTH), SSZ-35 (STF), SSZ-44 (SFF), Sigma-2 (SGT), SSZ-28 (DDR), and nonasil (NON).<sup>44</sup> By using potential energies from classical molecular dynamics (CMD) simulations to characterize interactions between guest template agents and host frameworks, Deem et al. predicted a viable OSDA candidate to synthesis the zeolite SSZ-52.<sup>45,46</sup> Muraoka et al. developed a *de novo* prediction model that can search efficiently for new OSDAs.<sup>47</sup> In a recent study by Gómez-Bombarelli et. al.,<sup>48</sup> a computational model of combining atomistic simulations, literature mining and experimental synthesis was proposed to enable the *a priori* control of phase selectivity in zeolite synthesis.

In all these previous studies where classical MD simulations were applied, the effect of electrostatic interactions between the OSDA and the lattice was ignored. That is, only the steric effects present between the OSDA and the zeolite framework were taken into account. Since we are interested in how the OSDA controls the resulting framework and Al distribution and siting, it is important to account for electrostatic interactions, since this undoubtedly plays a major role in how Al is distributed throughout the lattice. In this work, we combine classical and first-principles models to explore the dependence of charged OSDA/framework energies on the distribution of Al within the framework. We choose the zeolite CHA and the OSDA TMAda<sup>+</sup> as a model system. This is because CHA has a single, symmetry-distinct tetrahedra site, and TMAda<sup>+</sup> is known to form CHA. In addition, TMAda<sup>+</sup> can adopt only two geometrically equivalent but orientationally opposite configurations within the CHA cage, thereby reducing the total number of distinct OSDA orientations within

the lattice. We postulate that lattice energies are related to Al distribution for a given orientation of TMAda<sup>+</sup>, which if true suggests that OSDA/framework interactions are a potentially exploitable design parameter in creating zeolites enriched in desirable heteroatom configurations.

## 2 Simulation Details

### 2.1 Sampling Al Configurations and OSDA Orientations

Our hypothesis is that the potential energy between OSDAs and the CHA framework is related to the probability of a given Al configuration during synthesis. We therefore investigated the interaction energy between a pre-formed CHA framework with co-caged OSDAs. For the CHA framework with TMAda<sup>+</sup> as the OSDA, the Al distribution or “configuration”, the direction of the long axis of TMAda<sup>+</sup> as it sits in the framework or “OSDA orientation”, and the local position of the OSDA atoms “OSDA conformation”, can all have a significant effect on the energy. Two strategies were used to ensure that exhaustive sampling was done over all configurations, orientations, and conformations.

We first constructed a 36 T-site supercell using lattice constants obtained from the Database of Zeolite Structures.<sup>49</sup> Note that there are only two distinct ways that three TMAda<sup>+</sup> cations in a 36 T-site supercell can arrange themselves: all in the same orientation (which we denote “AAA”), and two TMAda<sup>+</sup> cations pointing in the same direction with the third pointing in the opposite directions (which we denote “AAB”). Three TMAda<sup>+</sup> cations were added to the CHA lattice in a given orientation. Following this, three Al atoms were distributed over all possible T-sites in the lattice, excluding those that contain Al-O-Al linkages, since this violates Löwenstein’s rule. This results in 4908 Al configurations for a given TMAda<sup>+</sup> orientation. By flipping the orientation of one TMAda<sup>+</sup> cation and placing Al atoms in all possible T-sites, another 4908 Al configurations were obtained, for a total of 9816 separate initial configurations.

Then, we carried out MD simulations on each of the 9816 configurations. The energy barrier for a TMAda<sup>+</sup> to “flip” from one orientation to the other is so high that on the timescale of the MD simulations, the TMAda<sup>+</sup> cations only sample their local conformations; they do not flip. The average potential energy  $\langle U \rangle_i$  of each configuration  $i$  was computed and the relative energy of each configuration  $\Delta U_i$  was computed as

$$\Delta U_i = (\langle U \rangle_i - U_{ref})/N_{D6R} \quad (1)$$

where the reference potential energy  $U_{ref}$  is taken as the lowest energy configuration

$$U_{ref} = \min_i \{ \langle U \rangle_i \} \quad (2)$$

and the energy is normalized by the number of double-six-ring (D6R) units in the simulated system. This enables comparison of results between different sized systems.

Chabazite has a high symmetry framework consisting of 8-member-rings (8-MRs), 6-member-rings (6-MRs) and 4-member-rings (4-MRs). The orientation of TMAda<sup>+</sup> and the Al configuration have the largest effect on the energy; the local conformations of TMAda<sup>+</sup> have a secondary effect on the overall energy. By sampling over all possible Al configurations and OSDA orientations, it is possible to identify high and low probability states. Note that due to the symmetry of the system, we sample degenerate states and the probability of a given state is determined from its Boltzmann weight. Comparison of energies obtained with the classical model and Born-Oppenheimer molecular dynamics simulations were made for a subset of the Al configurations and OSDA orientations.

## 2.2 AIMD Simulations

Born-Oppenheimer molecular dynamics simulations were performed on systems containing different Al configurations and OSDA orientations using VASP<sup>50</sup> with PAW potential<sup>51,52</sup> at the gamma point using a plane wave cutoff of 400 eV at PBE-D3 level.<sup>53,54</sup> Simulations

were run at 633 K in the canonical (NVT) ensemble, using a Nosé-Hoover thermostat with time constant of 100 fs. A 1 fs time step was used. Hydrogen atoms were replaced by deuterium atoms to allow a larger time step. Zeolite framework atoms (Si, Al and O) were kept frozen during the simulations. For each step, self-consistent-field (SCF) electronic energies were converged to  $10^{-5}$  eV. 10 ps simulations were conducted for all structures. For each structure, the first 2.5 ps of the trajectory was discarded and the remaining 7.5 ps of the trajectory was used to calculate the average potential energy.

## 2.3 Classical Force Field

We used the Dreiding force field<sup>55</sup> to represent intramolecular OSDA interactions, as well as van der Waals interactions between the zeolite framework and the OSDA. We chose the Dreiding force field because it has been shown to perform well when treating interactions between OSDAs and siliceous zeolite frameworks.<sup>45,46</sup> The Dreiding force field<sup>55</sup> has the following functional form

$$E_{total} = \sum_{bonds} K_b(b - b_{eq})^2 + \sum_{angles} K_\theta(\theta - \theta_{eq})^2 + \sum_{dihedrals} V_n[1 + \cos(n\phi - \gamma)] \\ + \sum_{i < j} \left\{ 4\epsilon_{ij} \left[ \left( \frac{r_{ij}}{\sigma_{ij}} \right)^{12} - \left( \frac{r_{ij}}{\sigma_{ij}} \right)^6 \right] + \frac{q_i q_j}{4\pi\epsilon_0 r_{ij}} \right\} \quad (3)$$

We considered the Lennard-Jones (LJ) intramolecular and intermolecular interactions for TMAda<sup>+</sup>s but neglected self-interactions of the zeolite framework atoms since the lattice is rigid.

To model electrostatic interactions between the OSDA and the framework, we introduced partial charges into the system. To derive the partial charges, we performed three DFT minimization simulations starting from three different Al configurations and TMAda<sup>+</sup> orientations. Then the Density Derived Electrostatic and Chemical (DDEC) approach<sup>56,57</sup> was used to obtain atomic net charges for the three conformations. Plane-wave, periodic supercell DFT calculations were performed using the Vienna Ab initio Simulation Package

(VASP), version 5.4.1<sup>50</sup> to derive atomic charges. Projector augmented wave (PAW) treatment of core-valence interactions<sup>51,52</sup> was used and the first Brillouin zone was sampled at the gamma point only. All calculations were carried out at the Perdew-Burke-Ernzerhof (PBE) generalized gradient approximation (GGA)<sup>53</sup> level and using a plane wave cutoff of 400 eV with D3 method for van der Waals interactions (TS-vdW).<sup>54</sup> Structures used for charge analysis were optimized with SCF electronic energies converging to  $10^{-6}$  eV and atomic forces to less than 0.03 eV/Å (CONTCARs included in the Supporting Information). Then, single-point calculations were conducted to generate required AECCAR0, AECCAR2, and CHGCAR files for performing DDEC atomic population analysis.<sup>58</sup>

The partial charges derived in this way are robust; we performed ten additional minimizations on different configurations and orientations. The differences between the partial charges obtained from these two different sets of minimizations was less than 5%, and more importantly, the distribution of partial charges remained essentially the same. The XYZ files containing raw partial charges obtained from the different minimizations are provided as a zipped file in Supporting Information.

We then categorized the atomic charges based on their chemical environments. The partial charges used in this work are listed in table 1. For zeolite atoms, it is clear from the charges on Al and Si that the Al T-site has a different chemical environment than the Si T-site. So we reserved two atom types for Al and its adjacent O in the tetrahedra  $\text{AlO}_4^-$ , namely al and ob in the table 1 and fig. 1. The chemical environment of Si atoms can also be affected by the number of neighboring  $\text{AlO}_4^-$  groups, so the adjacent Si atoms were also divided into four types accordingly. For the TMAda<sup>+</sup> ion, it is clear that its carbon and hydrogen atoms need to be categorized based on their relative positions to the quaternary ammonium group. The definition of each atom type for TMAda<sup>+</sup> used in table 1 is illustrated in fig. 1. Atomic charges for chemically-equivalent atoms were summed and averaged from raw charge files, while neutrality of charges was also ensured during the process.



Table 1: Net atomic charges for zeolite and TMAda<sup>+</sup> atoms

Molecule	Atom type	$q(e)$	Molecule	Atom type	$q(e)$
CHA zeolite	al	1.79584	TMAda <sup>+</sup>	n	0.22348
	ob <sup>a</sup>	-1.05771		cnh	-0.30327
	oz <sup>b</sup>	-0.93365		hx	0.14625
	si <sup>c</sup>	1.84506		cn	0.20907
	si <sup>d</sup>	1.82378		cb	-0.27065
	si <sup>e</sup>	1.8025		hb	0.10192
	si <sup>f</sup>	1.78122		cj	0.05556
				hj	0.0712
				ce	-0.22186
				he	0.0907

<sup>a</sup> Bridging oxygen bonded to Al and Si.

<sup>b</sup> Bridging oxygen bonded 2 Si.

<sup>c</sup> Si without neighboring Al.

<sup>d</sup> Si with 1 neighboring Al.

<sup>e</sup> Si with 2 neighboring Al.

<sup>f</sup> Si with 3 neighboring Al.

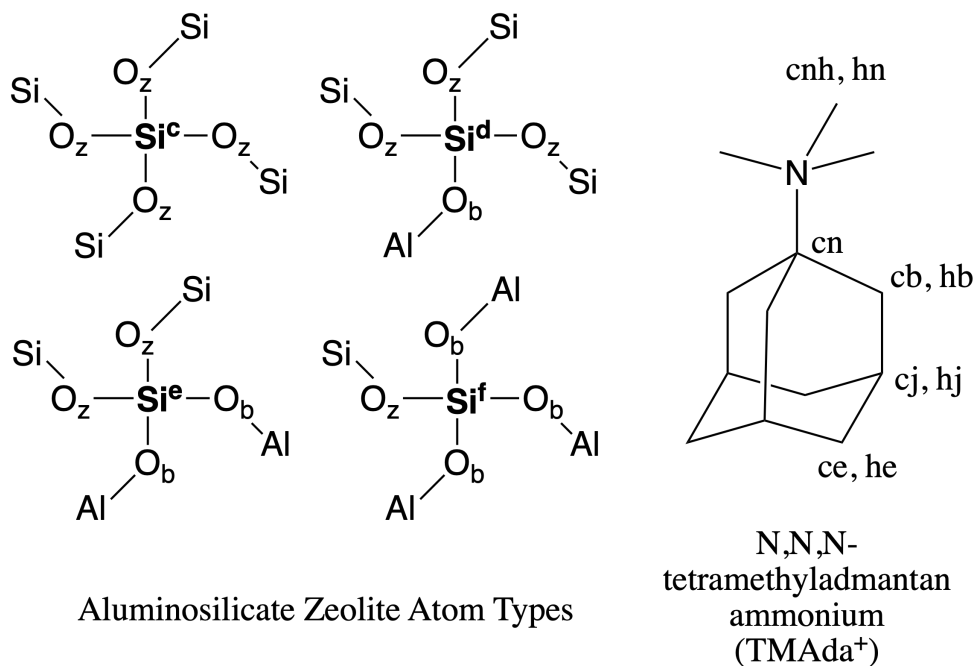


Figure 1: The structure of tetrahedra aluminosilicate unit, TMAda<sup>+</sup> and the definition of each atomic type used in table 1.

## 2.4 Classical Molecular Dynamics Simulations

In this study, we primarily investigate 36 T-site CHA systems with three pre-caged TMAda<sup>+</sup> ions. As discussed above, as the number of T-sites increases, the number of unique conformations goes up quickly. Limited by the computational cost of exploring each conformation, we only investigated a 36 T-site CHA supercell when considering all possible unique Al configurations and TMAda<sup>+</sup> orientations. The LAMMPS<sup>59</sup> package was used to carry out all classical molecular dynamics (CMD) simulations. Each simulation was equilibrated for 500 ps, followed by a production run of 1,500 ps with a time step of 0.2 fs. The NVT ensemble with the Nosé-Hoover<sup>60,61</sup> thermostat at 433K was applied. A cutoff of 10 Å was used for non-bonded interactions, including van der Waals attraction and repulsion, as well as electrostatic interactions. A standard long-range van der Waals tail correction was added to the energy and pressure, while a particle-particle particle-mesh solver<sup>62</sup> was applied to take care of the long-range electrostatic interaction.

## 3 Results and Discussion

### 3.1 Validating CMD results against DFT calculations

Before we analyzed the results of the CMD simulations (described below), we first needed to test the accuracy of the energies obtained from the CMD simulations. To do this, AIMD simulations were conducted on ten AAA and ten AAB systems having the lowest CMD energies and ten AAA and ten AAB systems with the highest CMD energies, for a total of forty systems. Initial structures for the AIMD simulations were obtained from the end of the 2 ns CMD trajectories of corresponding configurations and orientations. Initial VASP atomic nucleus position files (POSCARs) of these forty structures are included in the Supporting Information.

The AAB conformation that had the lowest CMD energy was chosen as the reference structure. CMD energies and AIMD energies of all forty structures normalized by the number of D6R units are plotted relative to the reference structure energy in fig. 2. CMD and AIMD energies along with uncertainties are listed in the Table S1 in Supporting Information. Uncertainties were taken as the standard deviation obtained from three equal length blocks of a single trajectory. CMD and AIMD energies show a linear correlation with an  $R^2$  of 0.95. CMD and AIMD results both show that the AAB orientation has an energy span of 60 kJ mol<sup>-1</sup> per D6R unit (180 kJ mol<sup>-1</sup> per 36 T-site supercell), while the AAA orientation has a much narrower energy span. The very different energy spans of AAA and AAB arrangements will be explained in detail below. The good agreement between CMD and AIMD potential energies suggests that the force field used in the CMD simulations is capable of adequately capturing energy trends.

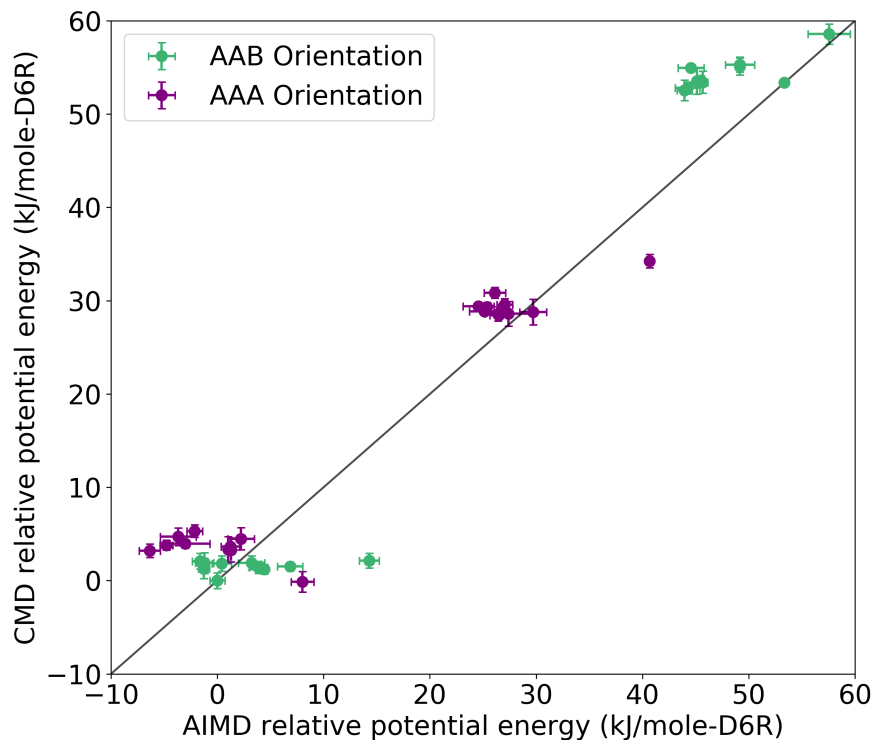


Figure 2: Comparison of AIMD and CMD potential energies (per D6R unit) of 10 lowest and 10 highest energy structures for AAA and AAB arrangements, respectively.

### 3.2 What are the most probable Al distributions in systems with the AAA TMAda<sup>+</sup> orientation?

On the left panel of fig. 3, we show an example snapshot including the CHA framework and the AAA orientated TMAda<sup>+</sup>s. In the middle panel, we report relative potential energies of different Al configurations, sorted from lowest to highest energy. Note that each point in the middle panel of fig. 3 corresponds to a specific Al configuration with the AAA orientated TMAda<sup>+</sup>s. We have divided the energy distribution into low, medium, and high energy regions (denoted by the dotted lines). The distribution was fit to a polynomial and the boundaries were set to where the second derivatives were zero. This resulted in 1499 configurations for the low energy region, 3098 configurations for the medium energy region,

and 311 configurations for the high energy region.

Each Al configuration has a specific distribution of Al atoms among different rings. We use this distribution to characterize each Al configuration. For a given 36 T-site CHA system, there are three Al sites and three TMAda<sup>+</sup>s. The three Al-Al pair combinations can take on the following distribution features: second nearest neighbors (NN) within an 8-MR; third NN within an 8-MR; fourth NN within an 8-MR; second NN within a 6-MR; third NN within a 6-MR; second NN within a 4-MR; both on a D6R unit; or isolated which includes all other scenarios. Figure 4 shows these Al pairs schematically.

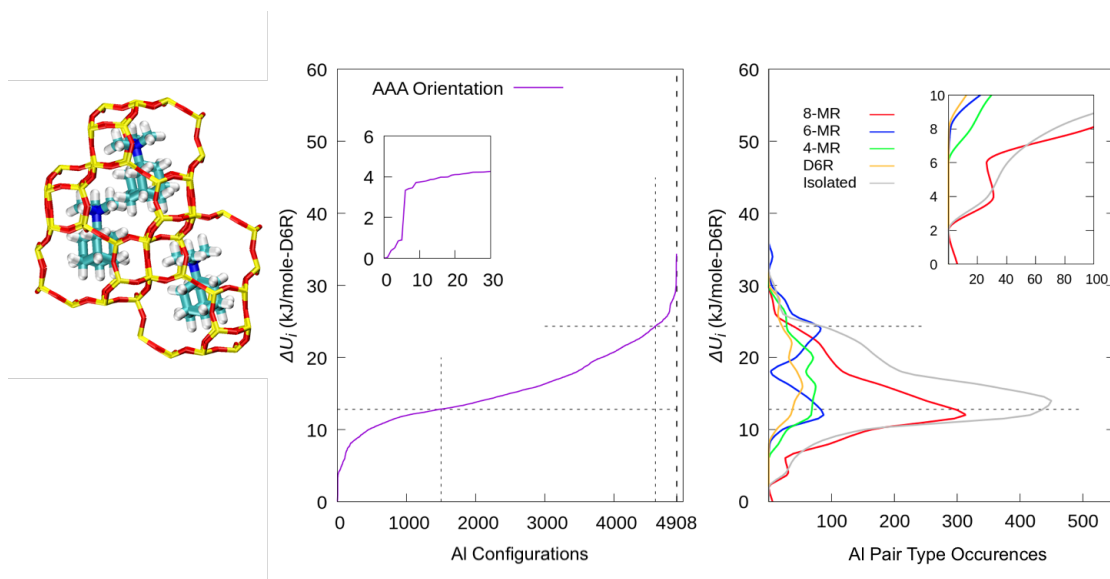


Figure 3: Relative potential energies ( $\Delta U_i$ ) of different Al configurations with the AAA TMAda<sup>+</sup> orientation. Note for left panel: extra framework atoms are shown to reflect the full cage in CHA; note for the middle panel: configurations are sorted by energies in ascending order.

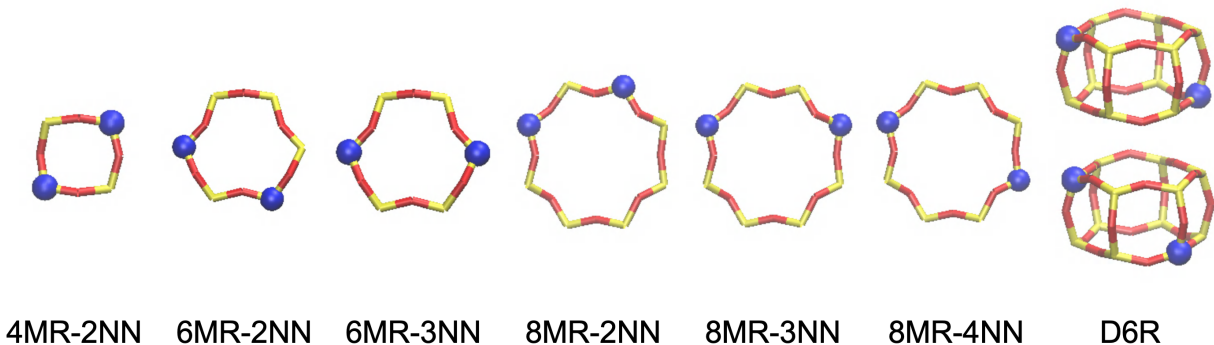


Figure 4: Schematic of Al ring pair types in the CHA zeolite framework. Isolated pairs are not shown.

In the right panel of fig. 3, the energy distribution of different Al pair types (8-MR, 6-MR, 4-MR, D6R and isolated) is shown. Because there are more combinations of 8-MR Al pairs, the area under the 8-MR curve is largest. The 8-MR pairs also have the lowest relative energies, with a significant fraction falling in the 0-4 kJ/mol-D6R range. Both suggest that, for a 36 T-site system with 3 Al atoms, the 8-MR pairs are favored. The 6-MR pairs have small energy peaks at approximately 12 and 25 kJ/mol-D6R, while the 4-MR and D6R pairs have broad energy distributions over 10-30 kJ/mol-D6R. Isolated Al pairs are more numerous than ring pairs, and have a broad distribution of energies.

To provide a sense of the types of Al pairs and their relative energies, we selected five representative low and high energy Al configurations. Figure 5 shows snapshots of the Al locations, along with their relative energies and Al pair type. All five low energy Al configurations have Al pairs on an 8-MR, while the five high energy Al configurations have Al pairs on the D6R unit, 6-MR or 4-MR. This observation is consistent with the energy distributions in fig. 3.

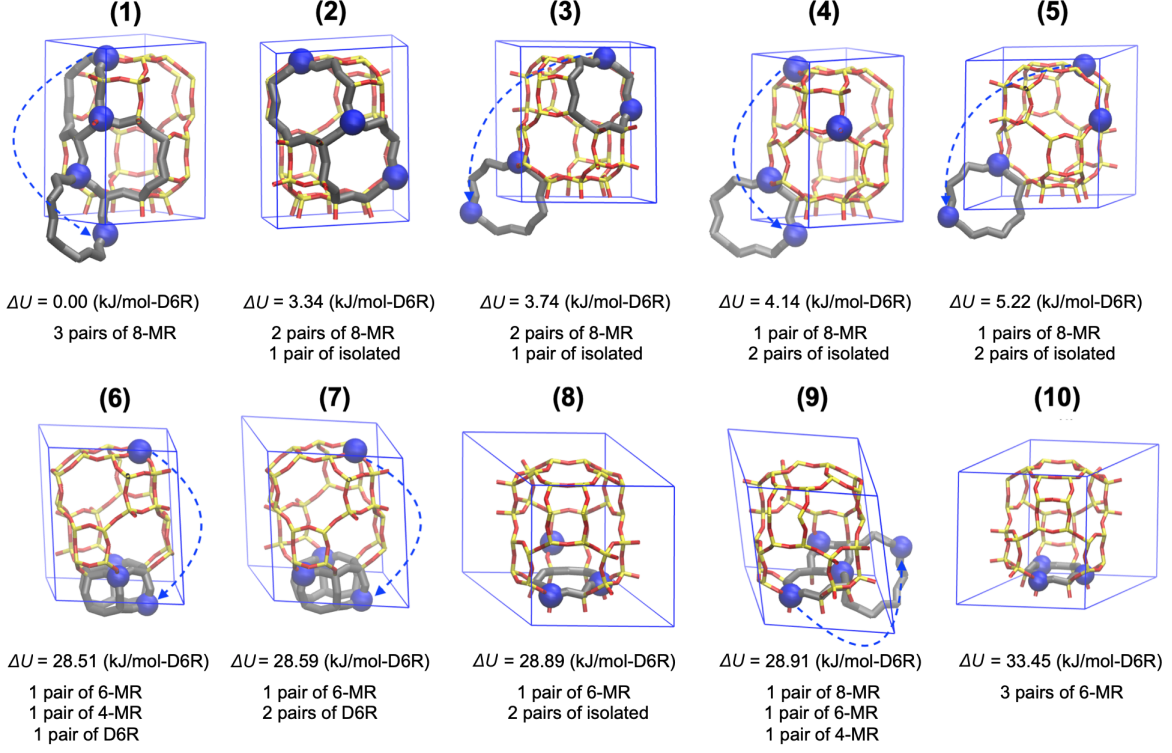


Figure 5: Example framework structures with the AAA TMAda<sup>+</sup> orientation. Extra framework atoms and Al from the nearby image are unwrapped to show a full Al-pair feature. The feature is highlighted in gray. Blue dashed arrows are showing the same Al unwrapped into different periodic images. Color: blue, Al; yellow, Si; red, O. (1)-(5) are Al pairs with low energies, while (6)-(10) are Al pairs with high energies.

To quantify the relative probabilities of different Al configurations, we performed Boltzmann weighting of each configuration. The configurational integral of the system with the AAA TMAda<sup>+</sup> orientation is

$$Z^{AAA} = \sum_i e^{-\Delta U_i/kT} \quad (4)$$

where  $i$  denotes an Al configuration,  $\Delta U_i$  is defined by eq. (1),  $k$  is the Boltzmann constant,  $T$  is the simulated temperature (433 K), and only AAA orientations are considered in the summation.

The probability of an Al configuration  $i$  with an AAA TMAda<sup>+</sup> orientation is

$$P_i = \frac{e^{-\Delta U_i/kT}}{Z^{AAA}} \quad (5)$$

Finally, the probability  $\Pi_j$  of a particular Al pair type  $j$  (i.e. 8-MR, 6-MR, 4-MR, D6R, or isolated) for an AAA TMAda<sup>+</sup> orientation is given by

$$\Pi_j = \sum_i \frac{n_{j,i}}{3} P_i \quad (6)$$

where the  $n_{j,i}$  stands for the number of Al pair types  $j$  in Al configuration  $i$ . The factor of 3 accounts for the fact that there are three Al pairs in each configuration.

Figure 6 shows the probabilities of each Al pair type. The left panel shows the overall Al pair type probability distribution for the AAA TMAda<sup>+</sup> orientation. The 8-MR and isolated pair types are by far the most probable, making up roughly 80% of the pair types. The 6-MR, 4-MR, and D6R pair types occur with low probabilities. The three other panels shows the pair type distributions in the low, medium, and high energy regions defined in fig. 3. As expected, the low and medium energy configurations are dominated by 8-MR and isolated pairs, while there is roughly equal probabilities of all Al pairs in the high energy region.

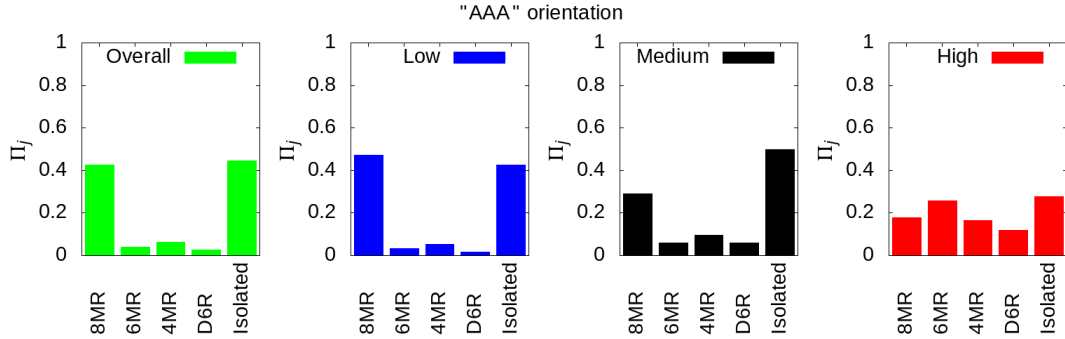


Figure 6: Probability distributions ( $\Pi_j$ ) of the AAA TMAda<sup>+</sup> orientations. Probability distributions are split into three regions with different colors, namely “low” (blue), “middle” (black), and “high” (red).



### 3.3 How different are Al distributions in systems with the AAB TMAda<sup>+</sup> orientation?

We next tested the sensitivity of the Al pair distributions to TMAda<sup>+</sup> orientation. We flipped the orientation of one TMAda<sup>+</sup> to obtain an AAB orientation and repeated the simulation procedure used for the AAA orientation. Energy distributions are reported in fig. 7. The lowest energy configurations for the AAB orientation have similar energies as the lowest energy configurations for the AAA orientation. However, the distribution of energies is much broader for the AAB orientation and there are more high energy configurations. There are more 6-MR, 4-MR, and D6R Al pairs that have low energies for the AAB orientation compared to the AAA orientation.

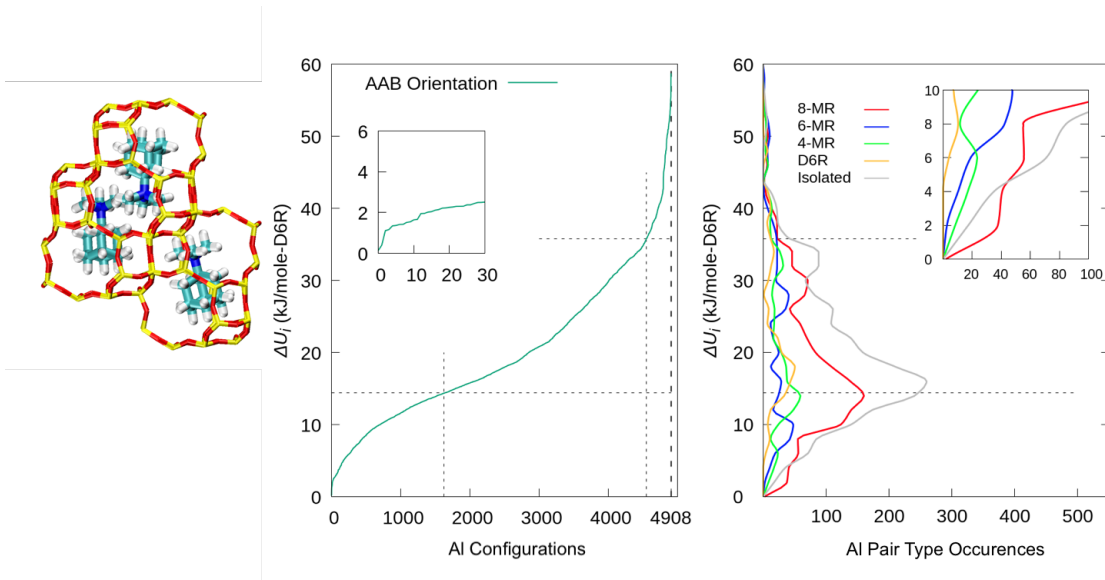


Figure 7: Relative potential energies ( $\Delta U_i$ ) of different Al configurations with the AAB TMAda<sup>+</sup> orientation. Note: configurations are sorted by energies in ascending order; extra framework atoms in the left panel are shown to reflect the full cage in CHA.

Figure 8 shows representative snapshots of low and high energy configurations, while fig. 9 shows the probabilities of Al pair types for the AAB orientation. The procedures for calculating these probabilities are the same as those described above for the AAA orientation. (1629, 2920 and 359 Al configurations for low energy, medium energy and high energy region,

respectively) Similar to the case with the AAA orientation, all five low energy snapshots have 8-MR Al pair types, but two of the low energy configurations also have 4-MR. The five high energy configurations consist of three 8-MR, five 6-MR, and three 4-MR totally.

Figure 9 shows the Al pair type probabilities for the AAB orientation. Overall, the probability distribution is similar to the AAA orientation, where the 8-MR and isolated Al pair types are the most probable. However, the number of 8-MR and isolated Al pair types in the high energy region is greater than 6-MR and 4-MR Al pair types, which is different than the AAA orientation. Although probability distributions of the AAA and AAB orientations are quantitatively different, they are qualitatively similar. Such probability distributions provide reasonable predictions against experiments,<sup>17</sup> where 6-MR and 4-MR, formed around those D6R units, are reported to be hardly detected in CHA from an OSDA(TMAda<sup>+</sup>)-only synthesis.

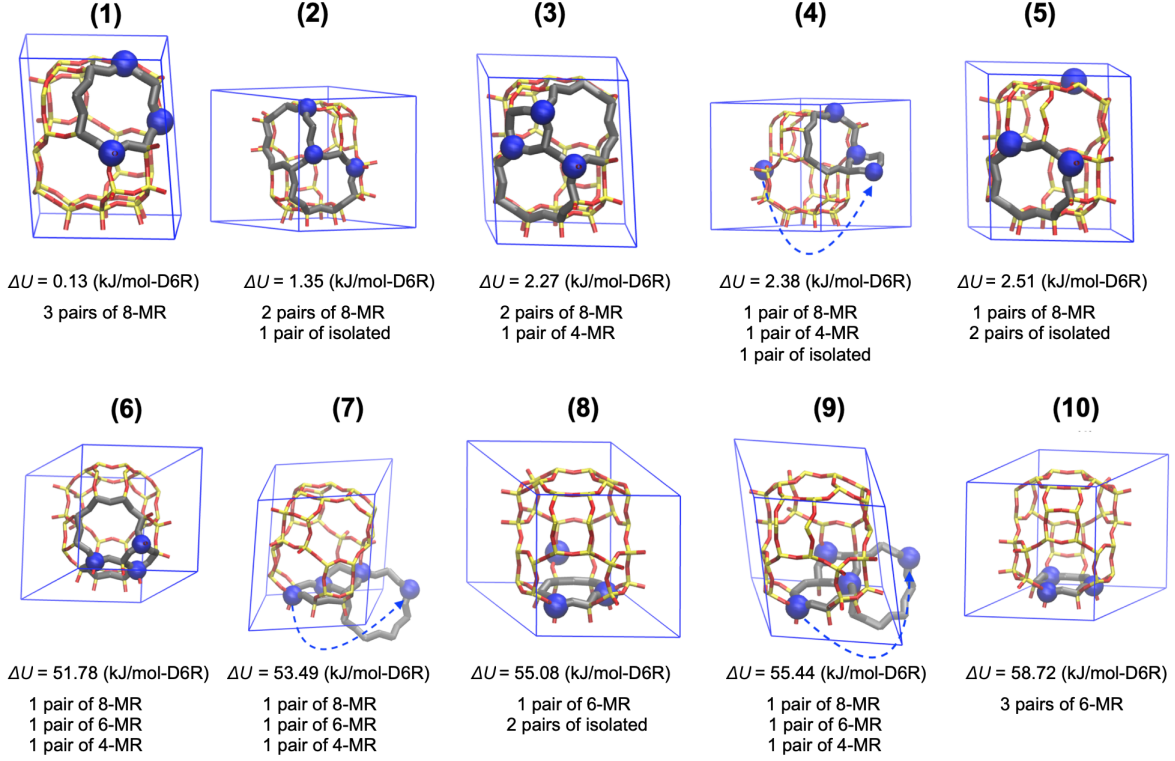


Figure 8: Example framework structures with the AAB TMAda<sup>+</sup> orientation. Extra framework atoms and Al from the nearby image are unwrapped to show a full Al-pair feature. The feature is highlighted by gray. Blue dashed arrows are showing same Al unwrapped into different periodic images. Color: blue, Al; yellow, Si; red, oxygen. (1)-(5) are frameworks with lower energies in fig. 7, while (6)-(10) are ones with higher energies.

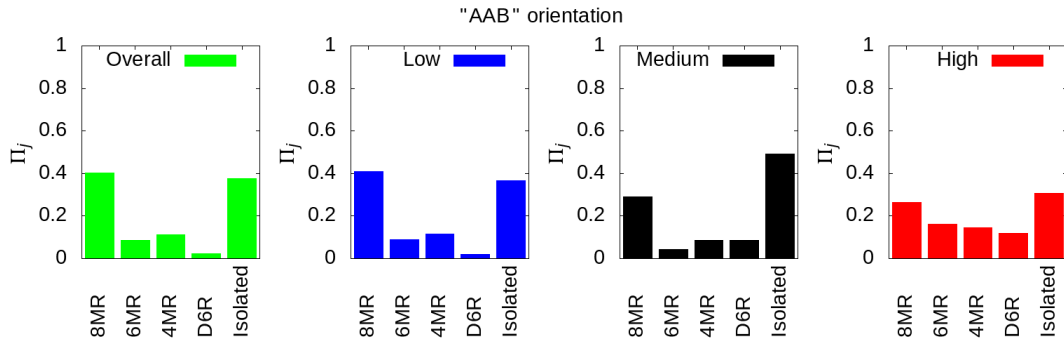


Figure 9: Probability distributions ( $\Pi_j$ ) of AAB TMAda<sup>+</sup> orientations. Probability distributions are split into three regions with different colors, namely “low” (blue), “medium” (black), and “high” (red). The way of grouping Al configurations is based on fig. 7 and has been discussed in the context.

### 3.4 What contributes most to the difference of the potential energy of each configuration?

We believe that the relative energies between different Al configurations is mainly related to the distance between Al atoms in the anionic tetrahedra  $\text{AlO}_4$  units and N atoms of the  $\text{TMAda}^+$ , due to electrostatic interactions. Figure 10 shows the distribution of Al-N distance for all Al configurations as a function of  $\text{TMAda}^+$  orientation. The AAB orientation has a broader distribution compared to the sharply peaked distribution for the AAA orientation. This is consistent with the energy distributions shown in fig. 3 and fig. 7.

To illustrate the underlying relation of Al-N distance to energy, fig. 11 shows a parity plot of averaged Al-N distances versus relative potential energies ( $\Delta U_i$ ) for the two  $\text{TMAda}^+$  orientations. There is a clear correlation between Al-N distance and relative energy, with the lower energy configurations have shorter Al-N distances. The AAA orientation has a much narrower energy and Al-N distance distribution than the AAB orientation, consistent with the results presented above. Parity plots of N-N distance versus  $\Delta U_i$ , as well as Al-Al distance versus  $\Delta U_i$  are provided in Figs S1, S2 in the Supporting Information. However, neither the N-N distance nor the Al-Al distance correlate well with the relative potential energy ( $\Delta U_i$ ). Though the potential energy can be a result of multiple contributions, among those, we believe that the cation-to-anion electrostatic interaction determined by Al-N distance contributes the most.

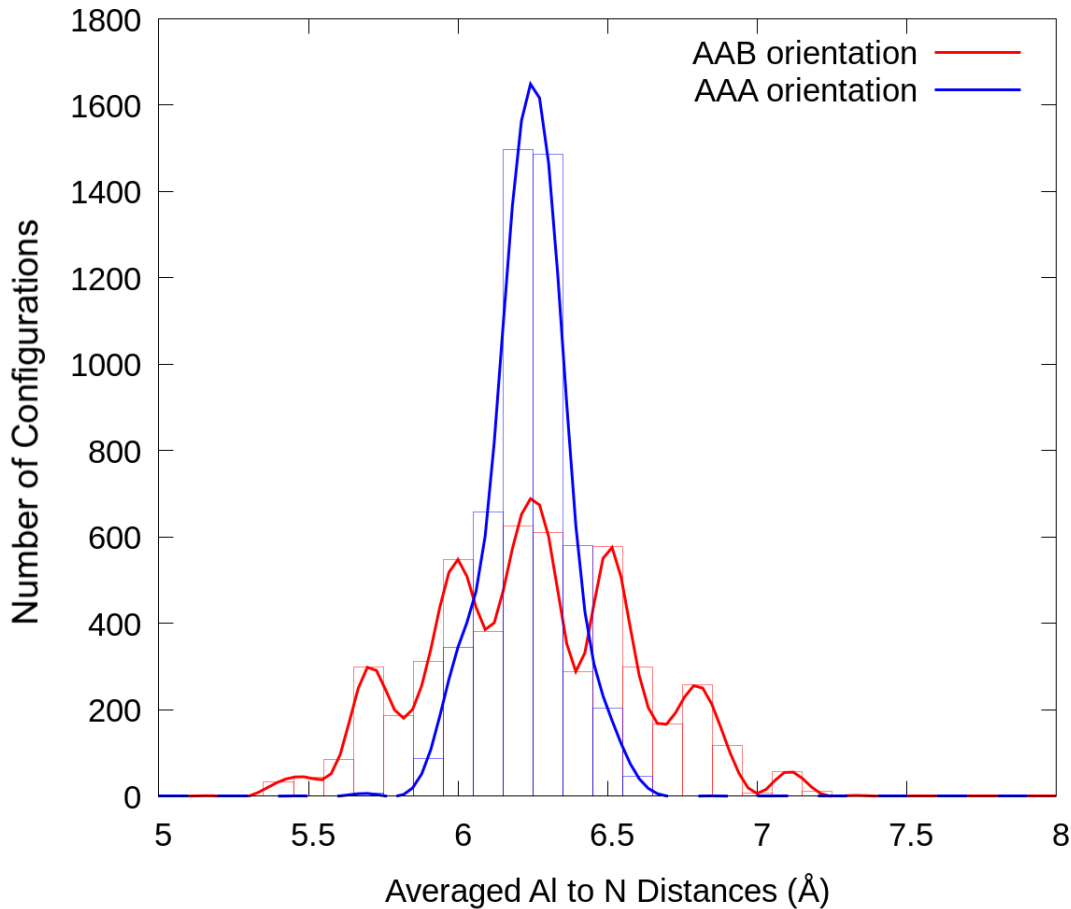


Figure 10: Averaged Al to quaternary ammonium N distance distributions for AAB (red) and AAA (blue). Note: there are 3 quaternary ammoniums and 3 Al sites, so the distance on the x-axis is the value averaged over 9 pairwise distances.

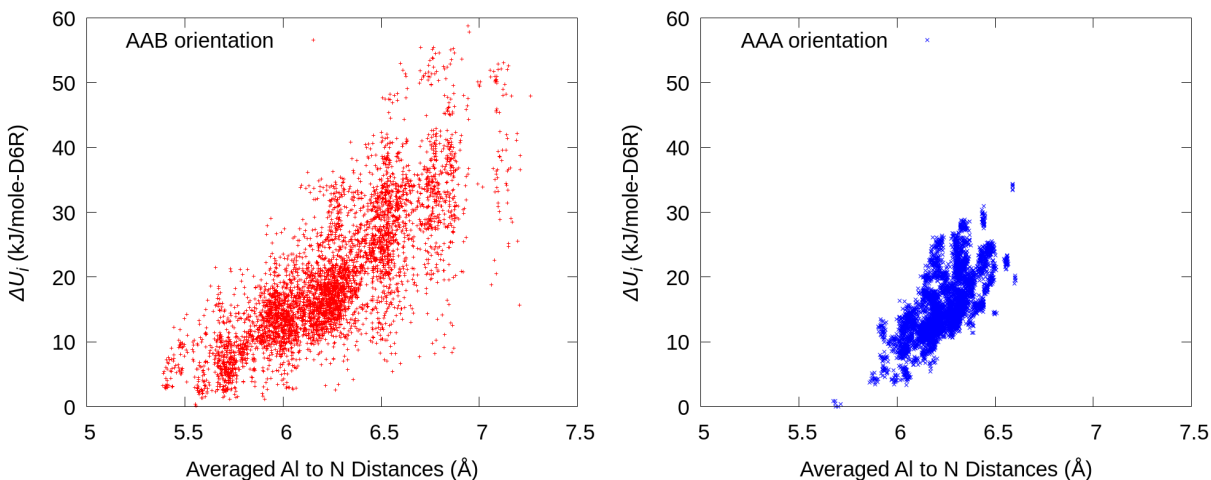


Figure 11: Averaged Al to quaternary ammonium N distances versus relative potential energies ( $\Delta U_i$ ). Left: “AAB” orientation in red. Right: “AAA” orientation in blue.

### 3.5 How does the TMAda<sup>+</sup> orientation affect the energy within a given framework structure?

To study the effect of TMAda<sup>+</sup> orientation on the energy of a given Al distribution, we selected two Al configurations from the AAA orientation in fig. 3 – one with the highest energy and the other with the lowest energy. With the Al distribution fixed, we flipped the orientation of each TMAda<sup>+</sup>, which resulted in 8 different orientations, some of which are degenerate, due to the symmetry of the framework. Figure 12 shows the two example frameworks, including their relative potential energies with respect to different TMAda<sup>+</sup> orientations. In the top panel, the three Al atoms are at each other’s 2-NN on 8-MRs. Among the relative potential energies in the top-right bar plot, we can observe that orientation #1 has the lowest energy (i.e. the reference energy of  $\Delta U_i = 0$  kJ/mol-D6R), while flipping the TMAda<sup>+</sup> orientation can lead to a energy increase of around 15 kJ/mol-D6R. In the bottom-right bar plot, in contrast, the highest energy ( $\sim 50$  kJ/mol-D6R) bar shows up at #2. However, flipping the orientation of TMAda<sup>+</sup>s now has an opposite effect which significantly reduces the energy to around 15 kJ/mol-D6R for #6. Experimentally, 3 Al residing on the same D6R, which is shown in the bottom-left panel of fig. 12, is not a preferable distribution.<sup>17</sup> But flipping the orientation of TMAda<sup>+</sup>s can stabilize the high energy framework by reducing the Al-N distance. Another interesting observation from comparing the two bar plots is that, although relative potential energies ( $\Delta U_i$ ) can be affected by the orientation of TMAda<sup>+</sup>, overall, all of the OSDA orientations associated with the low energy configuration are lower in energy than the high energy configurations, regardless of the orientation of TMAda<sup>+</sup>. This is consistent with the probability distributions in fig. 6 and fig. 9, where the probability distributions of Al pairs in AAA and AAB orientations are quantitatively different but qualitatively the same.

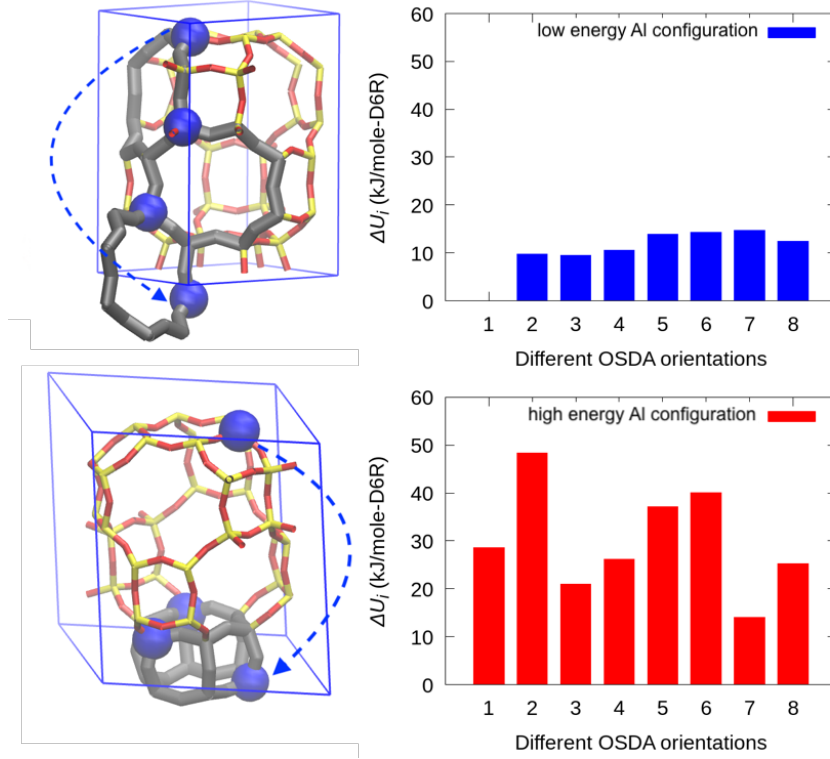


Figure 12: Bar plots of  $\Delta U_i$  for two sampled 36 T-site frameworks. Each bar in the plot represents a different TMAda<sup>+</sup> orientation. The blue bar plot on the top is generated from a low energy 36 T-site Al configuration, while the red bar plot on the bottom is from a high energy Al configuration. Schematics of the two configurations are shown on the left. Red: O; blue: Al; yellow: Si.

### 3.6 Effect of system size

Due to the high computational cost of these calculations, the majority of this work was limited to 36 T-site systems. To test whether the results obtained are sensitive to system size, additional calculations were performed on two 72 T-site systems. We selected the two Al configurations from fig. 12, one with the highest  $\Delta U_i$  and one with lowest  $\Delta U_i$ . Then, the lattice length was doubled along the  $\vec{c}$  lattice constant, which resulted in two different 72 T-site Al configurations. These two new Al configuration structures are shown schematically in fig. 13, along with bar plots showing the relative potential energies of different TMAda<sup>+</sup> orientations. For a given 72 T-site framework, there are 64 TMAda<sup>+</sup>-orientations, which results in 64 bars in fig. 13.

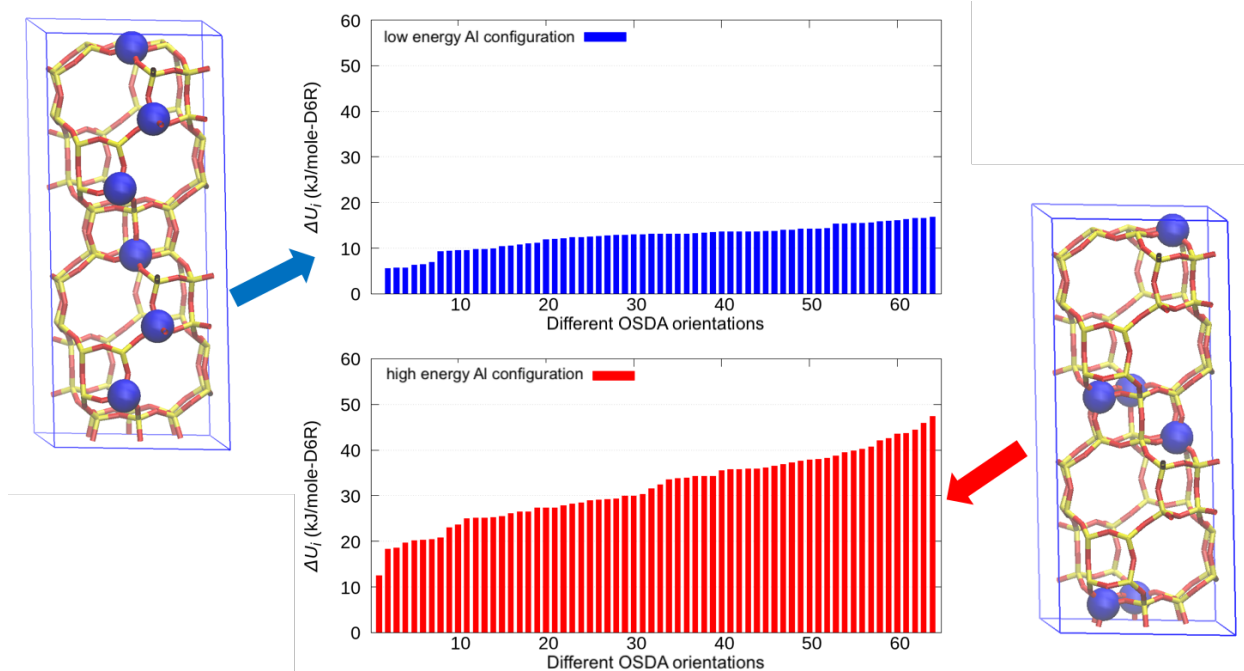


Figure 13: Bar plots of  $\Delta U_i$  for two sampled 72 T-site frameworks. Each bar in the plot represents a different TMAda<sup>+</sup> orientation. The blue bar plot on the top is generated by doubling the size of the lowest energy Al configuration from 36 T-site simulations. The red bar plot on the bottom is generated in the same way but with the highest potential energy. Red: O; blue: Al; yellow: Al. Note: to show the trend, potential energy bars are sorted in ascending order.

Similar to the results from the 36 T-site system, the different orientations of the low energy structure generally have lower energies than those obtained from the high energy structure. To compare results between the 36 T-site system and the 72 T-site system, energies were normalized by the number of D6R. The most important observation from fig. 13 is that the low energy Al configuration from 36 T-site simulations still has low potential energies in a larger supercell, regardless of the orientation of TMAda<sup>+</sup>s. In the larger supercell system, more asymmetric Al configurations will exist, so simply repeating 36 T-site systems is not able to ensure those conformations are adequately sampled. Due to the high computational cost of the brute force search method used in this work, a more efficient sampling approach, such as Monte Carlo, is needed to investigate larger systems. Alternatively, coarse graining could be performed to explore much larger systems.



## 4 Conclusions

In this work, we performed atomistic simulations to investigate how Al siting and OSDA position and orientation impacts the energy of a zeolite supercell. We examined a 36 T-site model of the CHA zeolite containing three  $\text{AlO}_4$  tetrahedral and 3  $\text{TMAda}^+$  OSDA molecules. We enumerated all possible Al configurations as well as  $\text{TMAda}^+$  positions and orientations. Classical molecular dynamics simulations were used to compute the average energy of each Al configuration as a function of  $\text{TMAda}^+$  orientation. In addition to van der Waals interactions between the zeolite lattice and the  $\text{TMAda}^+$ , electrostatic interactions were included by assigning partial charges to the framework atoms and the OSDA atoms using the DDEC partial charge method.

By applying a Boltzmann factor to each Al configuration and OSDA orientation, we came to the conclusion Al pairs prefer to locate in 8-MRs compared to 6-MR, 4-MR and D6R. This observation is consistent with our previous experimental finding that 6-MR are less likely to be found if the synthesis only involves  $\text{TMAda}^+$  as the OSDA without an inorganic SDA.<sup>17</sup> The main contribution to the potential energy comes from electrostatic interactions, which are governed by the distance between the anionic  $\text{AlO}_4$  tetrahedra and the cationic quaternary ammonium groups (the Al-N distance). Thus this is a key factor in determining the Al distribution in the lattice.

We also studied the influence of  $\text{TMAda}^+$  orientations on the energy of the Al distribution. The “AAB” orientation, where one  $\text{TMAda}^+$  is pointing in a different direction than the other two, has a broader energy distribution over all Al configurations than the “AAA” orientation.

Finally, we studied the effect of lattice system size by examining a 72 T-site lattice. Due to computational limitations, only two Al configurations were studied. For each Al configurations, we flipped the orientation of  $\text{TMAda}^+$  to generate 64 distinct orientations. Consistent with the findings from the 36 T-site system and regardless of the orientation of  $\text{TMAda}^+$ , the Al-N distance was found to govern the overall energy of the system.

The highlight of this work is the construction of a classical molecular model that probes the energy of an OSDA-zeolite system as a function of Al configuration and OSDA orientation. The results of the model are consistent with the experimental finding that Al tends to localize in 8-MR when TMA<sup>+</sup> is used as an OSDA in forming CHA. The insights of the model can help explain the energetic effects that lead an OSDA to help form a particular zeolite framework. In future work, we will use the model to: (1) include inorganic alkali structure directing agents and investigate their influence on Al distribution; (2) study other OSDAs and investigate their roles in shaping the formation of other aluminosilicate zeolites; (3) develop a Monte Carlo method to sample larger systems.

## Acknowledgement

The authors gratefully acknowledge the financial support from the National Science Foundation, CBET-DMREF under award number 1922154. The computing resources for this work were provided by the Notre Dame Center for Research Computing.

## Supporting Information Available

## References

- (1) Corma, A. State of the art and future challenges of zeolites as catalysts. *Journal of Catalysis* **2003**, *216*, 298–312.
- (2) Smit, B.; Maesen, T. L. Molecular simulations of zeolites: adsorption, diffusion, and shape selectivity. *Chemical reviews* **2008**, *108*, 4125–4184.
- (3) Qu, F.; Shi, R.; Peng, L.; Zhang, Y.; Gu, X.; Wang, X.; Murad, S. Understanding the effect of zeolite crystal expansion/contraction on separation performance of NaA

- zeolite membrane: A combined experimental and molecular simulation study. *Journal of Membrane Science* **2017**, *539*, 14–23.
- (4) Wang, X.; Zhang, Y.; Wang, X.; Andres-Garcia, E.; Du, P.; Giordano, L.; Wang, L.; Hong, Z.; Gu, X.; Murad, S., et al. Xenon recovery by DD3R zeolite membranes: application in anaesthetics. *Angewandte Chemie* **2019**, *131*, 15664–15671.
  - (5) Hinkle, K. R.; Wang, X.; Gu, X.; Jameson, C. J.; Murad, S. Computational molecular modeling of transport processes in nanoporous membranes. *Processes* **2018**, *6*, 124.
  - (6) Liu, C.; Tranca, I.; van Santen, R. A.; Hensen, E. J.; Pidko, E. A. Scaling relations for acidity and reactivity of zeolites. *The Journal of Physical Chemistry C* **2017**, *121*, 23520–23530.
  - (7) Haag, W.; Lago, R.; Weisz, P. The active site of acidic aluminosilicate catalysts. *Nature* **1984**, *309*, 589–591.
  - (8) Dědeček, J.; Sobalík, Z.; Wichterlová, B. Siting and distribution of framework aluminium atoms in silicon-rich zeolites and impact on catalysis. *Catalysis Reviews* **2012**, *54*, 135–223.
  - (9) Yilmaz, B.; Müller, U. Catalytic applications of zeolites in chemical industry. *Topics in Catalysis* **2009**, *52*, 888–895.
  - (10) Margeta, K.; Farkaš, A. Introductory Chapter: Zeolites-From Discovery to New Applications on the Global Market. *Zeolites-New Challenges* **2020**, 1–10.
  - (11) Gómez-Hortigüela, L.; Cambor, M. A. *Insights into the chemistry of organic structure-directing agents in the synthesis of zeolitic materials*; Springer, 2017; pp 1–41.
  - (12) Earl, D. J.; Deem, M. W. Toward a Database of Hypothetical Zeolite Structures. *Ind. & Eng. Chem. Res.* **2006**, *45*, 5449–5454.

- (13) Pinar, A. B.; Gomez-Hortiguera, L.; Perez-Pariente, J. Cooperative structure directing role of the cage-forming tetramethylammonium cation and the bulkier benzylmethylpyrrolidinium in the synthesis of zeolite ferrierite. *Chemistry of Materials* **2007**, *19*, 5617–5626.
- (14) Pinar, A. B.; Gómez-Hortigüela, L.; McCusker, L. B.; Perez-Pariente, J. Controlling the Aluminum Distribution in the Zeolite Ferrierite via the Organic Structure Directing Agent. *Chemistry of Materials* **2013**, *25*, 3654–3661.
- (15) Román-Leshkov, Y.; Moliner, M.; Davis, M. E. Impact of controlling the site distribution of Al atoms on catalytic properties in ferrierite-type zeolites. *The Journal of Physical Chemistry C* **2011**, *115*, 1096–1102.
- (16) Di Iorio, J. R.; Nimlos, C. T.; Gounder, R. Introducing Catalytic Diversity Into Single-Site Chabazite Zeolites of Fixed Composition via Synthetic Control of Active Site Proximity. *Acs Catalysis* **2017**, *7*, 6663–6674.
- (17) Di Iorio, J. R.; Gounder, R. Controlling the Isolation and Pairing of Aluminum in Chabazite Zeolites Using Mixtures of Organic and Inorganic Structure-Directing Agents. *Chemistry of Materials* **2016**, *28*, 2236–2247.
- (18) Paolucci, C.; Parekh, A. A.; Khurana, I.; Di Iorio, J. R.; Li, H.; Albarracin Caballero, J. D.; Shih, A. J.; Anggara, T.; Delgass, W. N.; Miller, J. T., et al. Catalysis in a Cage: Condition-Dependent Speciation and Dynamics of Exchanged Cu Cations in SSZ-13 Zeolites. *Journal of the American Chemical Society* **2016**, *138*, 6028–6048.
- (19) Dognier, F.; Patarin, J.; Guth, J.; Anglerot, D. Synthesis, characterization, and catalytic properties of silica-rich faujasite-type zeolite (FAU) and its hexagonal analog (EMT) prepared by using crown-ethers as templates. *Zeolites* **1992**, *12*, 160–166.
- (20) Lee, H.; Shin, J.; Lee, K.; Choi, H. J.; Mayoral, A.; Kang, N. Y.; Hong, S. B. Synthesis of thermally stable SBT and SBS/SBT intergrowth zeolites. *Science* **2021**, *373*, 104–107.

- (21) Sklenak, S.; Dědeček, J.; Li, C.; Wichterlová, B.; Gábová, V.; Sierka, M.; Sauer, J. Aluminum Siting in Silicon-Rich Zeolite Frameworks: A Combined High-Resolution  $^{27}\text{Al}$  NMR Spectroscopy and Quantum Mechanics/Molecular Mechanics Study of ZSM-5. *Angewandte Chemie* **2007**, *119*, 7424–7427.
- (22) Sklenak, S.; Dědeček, J.; Li, C.; Wichterlova, B.; Gabova, V.; Sierka, M.; Sauer, J. Aluminium siting in the ZSM-5 framework by combination of high resolution  $^{27}\text{Al}$  NMR and DFT/MM calculations. *Physical Chemistry Chemical Physics* **2009**, *11*, 1237–1247.
- (23) Dedecek, J.; Lucero, M. J.; Li, C.; Gao, F.; Klein, P.; Urbanova, M.; Tvaruzkova, Z.; Sazama, P.; Sklenak, S. Complex analysis of the aluminum siting in the framework of silicon-rich zeolites. A case study on ferrierites. *The Journal of Physical Chemistry C* **2011**, *115*, 11056–11064.
- (24) Yokoi, T.; Mochizuki, H.; Namba, S.; Kondo, J. N.; Tatsumi, T. Control of the Al distribution in the framework of ZSM-5 zeolite and its evaluation by solid-state NMR technique and catalytic properties. *The Journal of Physical Chemistry C* **2015**, *119*, 15303–15315.
- (25) Yokoi, T.; Mochizuki, H.; Biligetu, T.; Wang, Y.; Tatsumi, T. Unique Al distribution in the MFI framework and its impact on catalytic properties. *Chemistry Letters* **2017**, *46*, 798–800.
- (26) Biligetu, T.; Wang, Y.; Nishitoba, T.; Otomo, R.; Park, S.; Mochizuki, H.; Kondo, J. N.; Tatsumi, T.; Yokoi, T. Al distribution and catalytic performance of ZSM-5 zeolites synthesized with various alcohols. *Journal of Catalysis* **2017**, *353*, 1–10.
- (27) Vjunov, A.; Fulton, J. L.; Huthwelker, T.; Pin, S.; Mei, D.; Schenter, G. K.; Govind, N.; Camaioni, D. M.; Hu, J. Z.; Lercher, J. A. Quantitatively probing the Al distribution in zeolites. *Journal of the American Chemical Society* **2014**, *136*, 8296–8306.

- (28) Han, O. H.; Kim, C.-S.; Hong, S. B. Direct Evidence for the Nonrandom Nature of Al Substitution in Zeolite ZSM-5: An Investigation by  $^{27}\text{Al}$  MAS and MQ MAS NMR. *Angewandte Chemie International Edition* **2002**, *41*, 469–472.
- (29) Kim, C. W.; Heo, N. H.; Seff, K. Framework Sites Preferred by Aluminum in Zeolite ZSM-5. Structure of a Fully Dehydrated, Fully  $\text{Cs}^{+}$ -Exchanged ZSM-5 Crystal (MFI,  $\text{Si}/\text{Al} = 24$ ). *The Journal of Physical Chemistry C* **2011**, *115*, 24823–24838.
- (30) Mentzen, B. F.; Bergeret, G. Crystallographic determination of the positions of the copper cations in zeolite MFI. *The Journal of Physical Chemistry C* **2007**, *111*, 12512–12516.
- (31) Van Bokhoven, J. A.; Lee, T.-L.; Drakopoulos, M.; Lamberti, C.; Thieß, S.; Zegenhagen, J. Determining the aluminium occupancy on the active T-sites in zeolites using X-ray standing waves. *Nature Materials* **2008**, *7*, 551–555.
- (32) Bohinc, R.; Hoszowska, J.; Dousse, J.-C.; Błachucki, W.; Zeeshan, F.; Kayser, Y.; Nachtegaal, M.; Pinar, A. B.; van Bokhoven, J. A. Distribution of aluminum over different T-sites in ferrierite zeolites studied with aluminum valence to core X-ray emission spectroscopy. *Physical Chemistry Chemical Physics* **2017**, *19*, 29271–29277.
- (33) Perea, D. E.; Arslan, I.; Liu, J.; Ristanović, Z.; Kovarik, L.; Arey, B. W.; Lercher, J. A.; Bare, S. R.; Weckhuysen, B. M. Determining the location and nearest neighbours of aluminium in zeolites with atom probe tomography. *Nature communications* **2015**, *6*, 1–8.
- (34) Nicholas, J. B. Density functional theory studies of zeolite structure, acidity, and reactivity. *Topics in Catalysis* **1997**, *4*, 157–171.
- (35) Blaszkowski, S. R.; van Santen, R. A. The mechanism of dimethyl ether formation from methanol catalyzed by zeolitic protons. *Journal of the American Chemical Society* **1996**, *118*, 5152–5153.

- (36) Krossner, M.; Sauer, J. Interaction of water with Brønsted acidic sites of zeolite catalysts. Ab initio study of 1: 1 and 2: 1 surface complexes. *The Journal of Physical Chemistry* **1996**, *100*, 6199–6211.
- (37) Sierka, M.; Sauer, J. Structure and reactivity of silica and zeolite catalysts by a combined quantum mechanics - shell-model potential approach based on DFT. *Faraday Discussions* **1997**, *106*, 41–62.
- (38) Schröder, K.-P.; Sauer, J. Potential functions for silica and zeolite catalysts based on ab initio calculations. 3. A shell model ion pair potential for silica and aluminosilicates. *The Journal of Physical Chemistry* **1996**, *100*, 11043–11049.
- (39) Catlow, C.; Sinclair, P.; Sokol, A. A model for the formation of point defects in zeolites. *Radiation Effects and Defects in Solids* **1999**, *151*, 235–241.
- (40) Fletcher, R. E.; Ling, S.; Slater, B. Violations of Löwenstein’s Rule in Zeolites. *Chemical Science* **2017**, *8*, 7483–7491.
- (41) Li, S.; Gounder, R.; Debellis, A.; Müller, I. B.; Prasad, S.; Moini, A.; Schneider, W. F. Influence of the N, N, N-Trimethyl-1-adamantyl Ammonium Structure-Directing Agent on Al Substitution in SSZ-13 Zeolite. *The Journal of Physical Chemistry C* **2019**, *123*, 17454–17458.
- (42) Di Iorio, J. R.; Li, S.; Jones, C. B.; Nimlos, C. T.; Wang, Y.; Kunkes, E.; Vattipalli, V.; Prasad, S.; Moini, A.; Schneider, W. F., et al. Cooperative and Competitive Occlusion of Organic and Inorganic Structure-Directing Agents within Chabazite Zeolites Influences Their Aluminum Arrangement. *Journal of the American Chemical Society* **2020**, *142*, 4807–4819.
- (43) Lewis, D. W.; Willock, D. J.; Catlow, C. R. A.; Thomas, J. M.; Hutchings, G. J. De Novo Design of Structure-Directing Agents for the Synthesis of Microporous Solids. *Nature* **1996**, *382*, 604–606.

- (44) Burton, A. W.; Lee, G. S.; Zones, S. I. Phase selectivity in the syntheses of cage-based zeolite structures: An investigation of thermodynamic interactions between zeolite hosts and structure directing agents by molecular modeling. *Microporous and mesoporous materials* **2006**, *90*, 129–144.
- (45) Pophale, R.; Daeyaert, F.; Deem, M. W. Computational Prediction of Chemically Synthesizable Organic Structure Directing Agents for Zeolites. *Journal of Materials Chemistry A* **2013**, *1*, 6750–6760.
- (46) Davis, T. M.; Liu, A. T.; Lew, C. M.; Xie, D.; Benin, A. I.; Elomari, S.; Zones, S. I.; Deem, M. W. Computationally Guided Synthesis of SSZ-52: A Zeolite for Engine Exhaust Clean-Up. *Chemistry of Materials* **2016**, *28*, 708–711.
- (47) Muraoka, K.; Chaikittisilp, W.; Okubo, T. Multi-Objective de Novo Molecular Design of Organic Structure-Directing Agents for Zeolites Using Nature-Inspired Ant Colony Optimization. *Chemical Science* **2020**, *11*, 8214–8223.
- (48) Schwalbe-Koda, D.; Kwon, S.; Paris, C.; Bello-Jurado, E.; Jensen, Z.; Olivetti, E.; Willhammar, T.; Corma, A.; Román-Leshkov, Y.; Moliner, M.; Gómez-Bombarelli, R. A priori control of zeolite phase competition and intergrowth with high-throughput simulations. *Science* **2021**, eabh3350.
- (49) Baerlocher, C.; McCusker, L. Database of Zeolite Structures. <http://www.iza-structure.org/databases/>.
- (50) Kresse, G.; Furthmüller, J. Efficient iterative schemes for ab initio total-energy calculations using a plane-wave basis set. *Phys. Rev. B* **1996**, *54*, 11169–11186.
- (51) Blöchl, P. E. Projector augmented-wave method. *Phys. Rev. B* **1994**, *50*, 17953–17979.
- (52) Kresse, G.; Joubert, D. From ultrasoft pseudopotentials to the projector augmented-wave method. *Phys. Rev. B* **1999**, *59*, 1758–1775.



- (53) Perdew, J. P.; Wang, Y. Accurate and simple analytic representation of the electron-gas correlation energy. *Phys. Rev. B* **1992**, *45*, 13244–13249.
- (54) Grimme, S.; Antony, J.; Ehrlich, S.; Krieg, H. A consistent and accurate ab initio parametrization of density functional dispersion correction (DFT-D) for the 94 elements H-Pu. *The Journal of Chemical Physics* **2010**, *132*, 154104.
- (55) Mayo, S. L.; Olafson, B. D.; Goddard, W. A. DREIDING: a generic force field for molecular simulations. *Journal of Physical chemistry* **1990**, *94*, 8897–8909.
- (56) Manz, T. A.; Sholl, D. S. Chemically meaningful atomic charges that reproduce the electrostatic potential in periodic and nonperiodic materials. *Journal of Chemical Theory and Computation* **2010**, *6*, 2455–2468.
- (57) Manz, T. A.; Sholl, D. S. Improved atoms-in-molecule charge partitioning functional for simultaneously reproducing the electrostatic potential and chemical states in periodic and nonperiodic materials. *Journal of chemical theory and computation* **2012**, *8*, 2844–2867.
- (58) Manz, T. A. USER’S GUIDE Chargemol program for performing DDEC atomic population analysis. <https://sourceforge.net/projects/ddec//>.
- (59) Plimpton, S. Fast parallel algorithms for short-range molecular dynamics. *Journal of computational physics* **1995**, *117*, 1–19.
- (60) Nosé, S. A unified formulation of the constant temperature molecular dynamics methods. *The Journal of chemical physics* **1984**, *81*, 511–519.
- (61) Hoover, W. G. Canonical dynamics: Equilibrium phase-space distributions. *Physical review A* **1985**, *31*, 1695.
- (62) Hockney, R. W.; Eastwood, J. W. *Computer simulation using particles*; crc Press, 2021.